

Direct numerical simulations of riblets to constrain the growth of turbulent spots

JAMES S. STRAND† AND DAVID B. GOLDSTEIN

Department of Aerospace Engineering and Engineering Mechanics,
The University of Texas at Austin, Austin, TX 78712, USA

(Received 7 May 2009; revised 7 September 2010; accepted 8 September 2010)

A spectral direct numerical simulation (DNS) code was used to study the growth and spreading of turbulent spots in a nominally laminar, zero-pressure-gradient boundary layer. In addition to the flat-plate case, the interaction of these spots with riblets was investigated. The flat plate, riblets and initial spot perturbation were simulated via an immersed boundary method, and a ‘suction wall’ allowed the available channel code to model a boundary layer. In both flat-wall and riblet cases, self-similar arrowhead-shaped spots formed. The λ_2 variable of Jeong & Hussain (1995) was used to visualize the vortical structures within a spot, and a spot was seen to consist primarily of a multitude of entwined hairpin vortices. The range of scales of the hairpin vortices was found to increase as the spot matures. Ensemble averaging was used to obtain more accurate results for the spot spreading angle, both for the flat-wall case and the riblet case. The spreading angle for the flat-wall spot was 6.3° , in reasonably good agreement with prior DNS work. The spreading angle for the spot over riblets was 5.4° , a decrease of 14 % compared with the flat-wall.

Key words: Drag reduction, Transition to turbulence

1. Introduction

1.1. *Turbulent spots*

For values of the Reynolds number based on x which are relatively low ($Re_x = U_\infty x / \nu < 10^5$ – 10^6 for a flat plate), the boundary layer near a solid wall will remain laminar. As Re_x increases, a flat-plate boundary layer becomes increasingly unstable, and transition to turbulence will eventually occur. As Tollmien–Schlichting (T–S) waves in a boundary layer grow to large amplitudes, secondary instabilities develop and turbulent spots form. These spots take on an arrowhead shape, pointing downstream. Emmons (1951) was the first to describe these spots, and for this reason they are sometimes referred to as Emmons spots. The spots appear at randomly distributed points and their growth and merging lead to complete transition to turbulence. A spot appears as a fairly well-defined region of turbulence surrounded by laminar flow.

Turbulent spots can also be artificially generated with a localized perturbation in a laminar boundary layer. Artificially generated spots have been investigated by both experiments and direct numerical simulation (DNS). Schubauer & Klebanoff (1955) studied both naturally occurring and artificially generated spots in a low-disturbance

† Email address for correspondence: strand_js@yahoo.com

wind tunnel. In order to generate spots artificially, they used an electrical spark for the localized perturbation. Elder (1960) also used a spark to trigger turbulent spots on a flat plate in a wind tunnel. His examination of data from hot-wire measurements, along with flow visualization performed in a water channel, led him to conclude that 'the region of turbulent flow on a flat plate is simply the sum of the areas that would be obtained if all spots grew independently'. In other words, a turbulent boundary layer is simply the superposition of a number of turbulent spots. Elder also argued that there is a 'critical intensity' of the velocity perturbation which is used to trigger the spot. If this intensity is not reached (as a result of the spark not being strong enough), then no spot will form.

Wynanski, Sokolov & Friedman (1976) studied artificially generated spots in greater detail, again with an electrical spark for the perturbation. Like Elder (1960), they found that if the perturbation was not strong enough, it was possible that no spot would develop. However, if a spot did form, it exhibited self-similar growth, independent of the initial perturbation. Wave packets, which they believed to be T-S waves, were observed near the upstream lateral edges of the spot. Wynanski, Zilberman & Haritonidis (1982) hypothesized that the breakdown of these wave packets led to the formation of eddies near the spanwise edges of the spot, and thus that the waves were at least partially responsible for the growth of the spots. At the leading edge of the spot, a distinct overhang region was observed. In this region, the flow immediately above the wall remains laminar, but turbulent fluctuations associated with the spot are found farther from the wall.

Cantwell, Coles & Dimotakis (1978) used laser Doppler velocimetry to study the flow field along the centreline of a turbulent spot over a plate in a water channel. They postulated a conical growth rate for the spot and used a similarity transformation based on this conical growth assumption to examine structures along the spot centreline. They make the further assumptions that meaningful particle paths can be determined from the ensemble-averaged velocity field and that the flow along the centreline is two-dimensional. With the aid of these assumptions, they conclude that strong entrainment occurs in the near-wall region at the front of the spot and also along the 'outer part of the rear interface' of the spot, and that 'the outer part of the forward interface' passively convects and does not entrain much fluid. Their argument that the overall spot is dominated by two large vortices is not supported by later DNS and experimental work.

Amini & Lespinard (1982) introduced a perturbation by injecting fluid through a hole in a flat plate by means of a loudspeaker. The vertical velocity induced directly above the hole by the injection was as high as $1.25U_\infty$ (where U_∞ is the free-stream velocity). They were primarily interested in studying a pre-turbulent spot, but their method of perturbation did generate the same arrowhead-shaped turbulent spots as other experiments. Using isodeviation contours of mean velocity, they estimated the spreading angle of the turbulent spot to be $\sim 10^\circ$ and the apex angle to be $\sim 30^\circ$. For an image of a turbulent spot, with spreading angle, apex angle, etc. labelled, see figure 1. Note that in figure 1, the spreading angle is measured from the location of the initial perturbation. It is also possible to measure the spreading angle from a virtual origin located upstream or downstream of the initial perturbation. The issue of how to define a virtual origin is discussed later in this work.

DNS has also been used to simulate turbulent spots. Henningson, Spalart & Kim (1987) used a spectral method to simulate the growth and spreading of a turbulent spot in an incompressible flat-plate boundary layer. The domain for these simulations was periodic in the streamwise and spanwise directions. To approximate the effect of

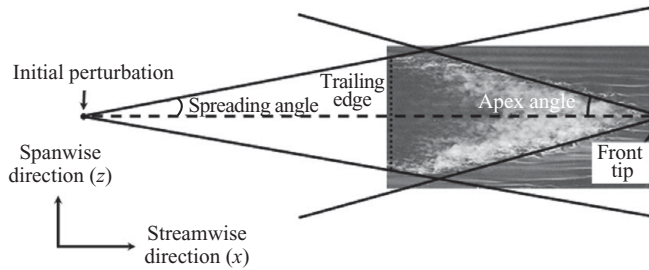


FIGURE 1. Schematic top view of a turbulent spot. The spot photograph used here was taken by R. E. Falco using smoke in a wind tunnel flow over a flat plate at $Re_x = 400\,000$ and was found in *An Album of Fluid Motion*, by Milton Van Dyke (1982), reproduced by kind permission.

the thickening of the surrounding boundary layer as the spot moves downstream, a weak body force was applied to the mean flow. The perturbation used to induce the spot was a localized, impulsive body force directed upstream. The spots generated with this perturbation exhibited self-similar growth, as found by experiments. Henningson *et al.* (1987) stated that ‘The turbulent vortical region grows at a half-angle of about 7° . The region in which the velocity is disturbed is wider, about 10° , in good agreement with experimental results’. It is not clear how they defined the edge of the *turbulent vortical region*, or how they defined the edge of the *disturbed region*. They found that the growth of the spot became self-similar after $t \approx 100\delta_o/U_\infty$ where δ_o is boundary layer 99% thickness at the location of the perturbation (the perturbation was initiated at $t = 0$). Once its growth became self-similar, the spot grew as if from a virtual origin at $t \approx 35\delta_o/U_\infty$ and $x \approx 15\delta_o$ (downstream of the initial perturbation). The trailing edge of the spot moved at $\sim 0.5U_\infty$ and the leading edge at $\sim 0.83U_\infty$. They note that these values compare reasonably well with the commonly quoted experimental values of $0.5U_\infty$ and $0.9U_\infty$, respectively. They also observed an overhang region at the leading edge of the spot, which is consistent with the experiments of Wagnanski *et al.* (1976).

Breuer & Landahl (1990) studied the evolution of a localized disturbance in a laminar, zero-pressure-gradient boundary layer. They noted the formation of intense shear layers and low-speed streaks and that the nonlinear portion of the disturbance grew rapidly. Many of the structures seen in their growing disturbance are similar to those seen in a fully turbulent boundary layer. Some of the structures are similar to three-dimensional lambda vortices, thus indicating that these vortices can form as part of a bypass transition mechanism, even without the presence and breakdown of T–S waves.

Singer & Joslin (1994) focused their DNS on the development of a turbulent spot in an incompressible, laminar, zero-pressure-gradient boundary layer. Their domain was periodic in the spanwise direction, and they used a buffer domain in the streamwise direction to allow for a non-reflective boundary condition on the streamwise velocity. Fluid injection through a short streamwise slot was used to perturb the flow and generate the hairpin vortex disturbance that grew into the turbulent spot. They note that some of the structures seen very soon after the fluid injection (especially the ‘U-shaped vortex’ and ‘necklace vortex’) are probably specific to the method of perturbation. Structures seen later appear to be more generic, such as the hairpin vortices which formed between the legs of other hairpins, and these structures would probably be a part of any young turbulent spot. In addition to the hairpins, a number of other ‘quasi-streamwise’ vortices were observed. Many of these quasi-streamwise

vortices initially formed under the legs of other streamwise vortices. The interaction of these quasi-streamwise vortices with high-pressure regions near the wall frequently led to an ejection of fluid away from the wall, and thus served as a method of vortex regeneration. Viscous entrainment of fluid by nearby vortices also led to the formation of new vortices in some cases, and new vortices were sometimes formed due to the rebound of fluid from the wall. Taken together, the above effects caused the disturbance to spread and grow into a young turbulent spot. They did not observe a wave packet near the wingtips of the spot, in agreement with the findings of Henningson *et al.* (1987). They did not report on the apex angle, spreading angle or leading-edge and trailing-edge speeds for the young spot.

Singer (1996) used the same code and method as that used by Singer & Joslin (1994) to further simulate the growth of the young turbulent spot. The simulated spot shared many characteristics with experimentally observed spots (such as those described by Wygnanski *et al.* 1976), including a distinct overhang region and a calm but non-Blasius region in the wake of the spot. As in the DNS of Henningson *et al.* (1987), no T–S waves were observed at the wingtips of the spot. Singer (1996) notes that the length of his domain in the streamwise direction is only about five times the typical T–S wavelength for the simulation Reynolds number. Furthermore, the calculation is run for less than four times the period of the highest frequency T–S wave for the simulation Reynolds number. Thus, he argues that T–S waves have neither enough time nor enough room to grow and propagate. A spatially averaged velocity profile does not show a distinct logarithmic region, but Singer states that the flow is probably beginning to develop a log layer. He notes some inconsistencies in the values which have been found by various experiments and simulations for the leading-edge and trailing-edge speeds and the spreading angle of turbulent spots. He attributes these inconsistencies primarily to the various methods used to define the edge of the spot. Some researchers have used isodeviation contours of the streamwise velocity to define the spot edge (this is the method used by Amini & Lespinaud 1982), while others (such as Henningson *et al.* 1987) have used specific isosurfaces of vorticity (or some other pertinent quantity). Singer (1996) defines the leading and trailing edges of the spot as the farthest downstream and upstream locations, respectively, at which the quantity $|\partial u/\partial x|$ along the spot centreline is greater than or equal to an arbitrary threshold value. He notes that this criterion leads to small jump discontinuities in the movement of the leading edge and larger discontinuities in the movement of the trailing edge. The spanwise edge is defined similarly, except that the edge is defined as the farthest spanwise point (at any x and y location), where the threshold is met. Again, this leads to multiple jump discontinuities, and thus Singer uses linear regression to define the leading-edge and trailing-edge speeds, and the spreading angle. He calculates a trailing-edge speed of $0.63U_\infty$ and a leading-edge speed of $0.94U_\infty$. For the spreading angle, he reports values of 3.8° or 6.4° , depending on whether the origin is defined as before or after a particularly large discontinuity in the plot of the spanwise extent of the spot versus the streamwise location of the spanwise edge. Although these values are significantly lower than previously reported experimental values, Singer (1996) argues that this is probably due to the fact that the Reynolds number (based on distance from the perturbation to the measurement location) was about 80 000, which is significantly lower in the simulation than in most experiments (Wygnanski *et al.* 1976 took some data at $Re_x = 120\,000$, but most of their data were for $Re_x = 600\,000$).

Krishnan & Sandham (2007) performed DNS of both isolated turbulent spots in a supersonic flat-plate boundary layer, and also the interaction of turbulent spots

with a shock-induced separation bubble. They found that the spots contained hairpin vortices, especially near the leading edge, and they noted the presence of quasi-streamwise vortices at the wingtips. Spot lateral spreading rates were greatly increased during the spot/bubble interactions. On the basis of these results, they proposed a conceptual model for spot lateral growth which is based on the destabilizing effect of the spot on the laminar boundary layer near the spot wingtips.

The DNS of the transition to turbulence of a flat-plate boundary layer performed by Wu & Moin (2008) also showed the presence of a large number of hairpin structures of various sizes within areas of turbulence inside the overall transition region.

Jocksch & Kleiser (2008) examined the development of turbulent spots in a simulated supersonic flat-plate boundary layer. They found that spots in this compressible flow have many of the same properties (e.g. arrowhead shape and overhang region at the front) as spots which are found in incompressible flow. Making use of λ_2 (the second invariant of the symmetric tensor $\mathbf{S}^2 + \mathbf{\Omega}^2$, where \mathbf{S} and $\mathbf{\Omega}$ are, respectively, the symmetric and antisymmetric parts of the velocity gradient tensor ∇u , Jeong & Hussain 1995), they identified multiple hairpin vortices within their spots. Semi-circular wave patterns are observed emanating from the core of the spot. However, the authors believe these waves to be an effect of compressibility, and they state that (Jocksch & Kleiser 2008, p. 1556) ‘we do not see a necessary connection of these waves in the near-field of turbulent spots with waves discussed previously in the literature that are associated with turbulent spots in incompressible boundary layers’.

Our recent work examined methods for properly defining the boundaries of a spot and calculated the spreading angle for spots over various surface textures (Strand & Goldstein 2007). This work was followed up by a more detailed study of different texture geometries (Strand 2007), which also made use of λ_2 for examination of the spot structure and suggested that a spot is composed primarily of a large number of hairpin vortical structures. Finally, spots were allowed to develop further in a larger domain in order to examine the spreading angle of more mature spots (Strand & Goldstein 2010). To the best of the authors’ knowledge, these spot simulations are the largest performed to date, both computationally ($\sim 110\,000\,000$ grid points) and in how far the spots were followed downstream of the initial perturbation ($Re_x \approx 50\,000$ at the location of the perturbation and $\sim 300\,000$ at the end of the domain).

1.2. Delaying transition

If one could delay the onset of transition, the benefits would be appreciable since the viscous drag of a turbulent boundary layer can be four or more times greater than that of a laminar layer. It has been found experimentally, as described by Coustols & Savill (1992), that passive surface textures such as streamwise riblets can reduce the turbulent drag on a surface by 5%–10%. Bruse *et al.* (1993) investigated the drag reduction possible with a wide range of surface textures, including streamwise fins (or blade riblets) and triangular (or sawtooth) riblets. They were able to achieve a drag reduction of up to 6% with triangular riblets and 9% with streamwise fins. For a given value of h^+ (the height of the textures non-dimensionalized by the local mean friction length scale), the drag reduction was strongly dependent on the ratio of texture height to crest-to-crest spacing (h/s). Optimal drag reduction occurred at $h/s \approx 0.7$ in the case of triangular riblets and at $h/s \approx 0.5$ in the case of streamwise fins. The sharpness of the riblet tip was also important, with sharper riblets providing greater drag reduction for a given h/s . Similarly, thinner fins (thickness/spacing = 0.01)

provided greater drag reduction than thicker fins (thickness/spacing=0.04) for a given h/s .

These experimental results were confirmed numerically by Goldstein, Handler & Sirovich (1995). Goldstein & Tuan (1998) also argued that riblets work by damping the near-wall spanwise fluctuations, in agreement with Bruse *et al.* (1993).

If this damping could slow the spanwise spreading of turbulent spots, riblets might be used to delay transition, since in many engineering applications the state of the boundary changes from laminar to turbulent through the growth and merging of turbulent spots. Furthermore, the riblets would only need to be present in the transition region, so the expense of installing and maintaining riblet film covering this area would be much lower than that associated with covering the entire turbulent region.

Chu, Strand & Goldstein (2010) used an intermittency model originated by Narasimha (1985) to show that, if the leading-edge speed and trailing-edge speed are held constant, a decrease in spot spreading angle translates directly into an increase in the length of the transition region, and thus a delay in the onset of full turbulence.

2. Numerical method

2.1. The force field model and spectral approach

There exist several approaches to simulating laminar and turbulent boundary layers over textured surfaces. Goldstein, Handler & Sirovich (1993) combined the spectral code described by Handler, Hendricks & Leighton (1989) (which is based on the spectral method of Kim, Moin & Moser 1987) with an immersed boundary technique, to allow for the simulation of laminar or turbulent flows over a multitude of stationary or moving solid surfaces. The approach is particularly flexible and has been successfully tested on a range of turbulent flow configurations over passive surface textures and active MEMS-like devices, as discussed by Goldstein *et al.* (1995), Goldstein & Tuan (1998) and Colmenero (2004). This technique for modelling an immersed boundary introduces a localized body force field into the Navier–Stokes equations. The force field is made to adapt to the flow and bring it to a specified velocity on the immersed boundary points. This adaptation takes place by means of a two-parameter control scheme, which provides feedback based on both the current velocity at the point and the prior history of the velocity at that point (an integral term). The vector equation for the control scheme is

$$\mathbf{F}(\mathbf{x}, t) = \alpha \int_0^t [\mathbf{U}(\mathbf{x}, t') - \mathbf{U}_{des}(\mathbf{x}, t')] dt' + \beta [\mathbf{U}(\mathbf{x}, t) - \mathbf{U}_{des}(\mathbf{x}, t)], \quad (2.1)$$

where $\mathbf{U}(\mathbf{x}, t)$ is the actual velocity vector at a given grid point which forms part of the immersed boundary, $\mathbf{U}_{des}(\mathbf{x}, t)$ is the desired velocity vector at that point, α and β are negative constants, and $\mathbf{F}(\mathbf{x}, t)$ is the body force vector which is applied in the region of that grid point. The gain parameters α and β are generally constant in time, but they may be functions of position. This same base-control scheme can be used for other purposes besides creating solid or moving surfaces, as discussed later in this section. For a more detailed explanation of the immersed boundary method employed here, see Goldstein *et al.* (1993).

2.2. Simulation of a boundary layer

The code described above was originally designed for channel flow, and some modifications were required to allow the simulation of a boundary layer. First, a buffer zone was added to create the desired inlet Blasius profile. The buffer zone

uses the same control scheme as the solid immersed boundaries, but unlike the solid boundaries, the buffer zone does not enforce the no-slip condition. Instead, it forces the flow to assume a Blasius profile for a specified location on a flat plate. In order to avoid directly affecting the flow outside the buffer zone, the α and β parameters in the control scheme are made spatially dependent. At any given location in the buffer zone, the velocity gain parameter, β , is taken as

$$\beta = 20 \times \exp(\{-24[(x - x_{centre})/L_{buff}]^2\}), \quad (2.2)$$

where x_{centre} is the x -location of the midpoint of the buffer zone and L_{buff} is the buffer zone length. The integral gain parameter, α , is zero except in the central third of the buffer zone, where

$$\alpha = 20 \times \exp(\{-240[(x - x_{centre})/L_{buff}]^2\}) \quad (2.3)$$

is used. This combination of gains makes for a somewhat ‘soft’ buffer zone, in the sense that the velocity is brought gradually to the correct value as the flow passes through the zone. This is in contrast to the solid-surface immersed boundaries, where the forces which are applied to the flow are large enough to force the velocity to zero very quickly. For example, even for the case of a fully developed turbulent spot interacting with riblets, the maximum velocity on any solid surface immersed boundary anywhere in the domain is less than 1% of U_∞ at all times during the spot simulation. For further information on the buffer zone technique used here, see Goldstein, Cohen & Levinski (2001).

If no further modifications are made to the original channel-flow code, a favourable pressure gradient develops in the streamwise direction and the boundary layer does not grow downstream as the Blasius solution predicts. This happens because even when the top surface of the computational domain (the top wall of the channel) is set to allow slip, it still permits no-through flow. There is always some small but finite vertical velocity above a flat plate in an infinite domain, even very far from the plate. This vertical velocity can be calculated from the Blasius solution, as described by White (1991):

$$V_{edge} = 0.86039 \sqrt{\frac{\nu U_\infty}{x}}. \quad (2.4)$$

Thus, in order to model the boundary layer, it is necessary to accommodate this vertical velocity. It is a fundamental aspect of the spectral channel-flow code used for this work that the top and bottom domain boundaries must be set to either no-slip or no-through flow. No other conditions are possible, and so a different type of boundary must be added inside the overall computational domain. To this end, an immersed boundary was placed below the top wall of the channel to force a suitable upflow. The vertical velocity at all points on this ‘suction wall’ is forced (by the control scheme described earlier) to be that predicted by the Blasius solution, thus allowing normal streamwise growth of the boundary layer. Unlike the solid-wall immersed boundaries, the suction wall only applies the body force in the vertical direction; it exerts no force in the spanwise or streamwise directions. This suction wall serves the same purpose as a small variation in area in a real wind tunnel, which is used to maintain a zero pressure gradient in a test section. The boundary layer can be made to grow as if from the leading edge of the plate (the plate starts at or near the end of the buffer zone) or the velocity can be set in the buffer zone to a Blasius profile for a given x -location on the plate. In either case, the profile will develop correctly downstream, as demonstrated in the first section of the Appendix.

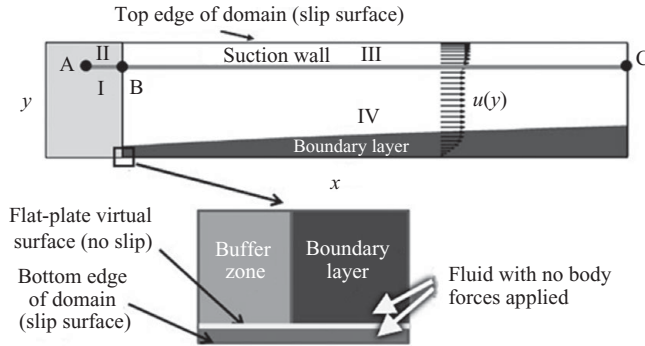


FIGURE 2. Schematic diagram of the computational domain with buffer zone and suction wall employed to model a Blasius boundary layer. Top image shows entire domain and is stretched in the y -direction but is otherwise to scale. Bottom image shows the virtual flat plate and the small area of fluid beneath it. Region IV is the region of interest in which the spots develop.

A schematic diagram in figure 2 shows the locations of the buffer zone, the suction wall and the flat-plate virtual surface. In the top image, the y -direction is exaggerated by 10 times compared with the x -direction for visual clarity, but with this scaling in mind, the dimensions are otherwise correct. Note that room is left between the suction wall and the top boundary of the domain. This is done because the fluid which is sucked through the wall has nowhere to go but downstream, and as more fluid is added along the length of the domain, the fluid above the suction wall is forced to accelerate. The smaller the space between the suction wall and the top boundary of the computational domain, the larger this acceleration. Therefore, some space must be left in order to avoid the need for an excessively small time step. This is not an issue near the bottom of the domain, since no fluid is being sucked through the no-slip immersed boundary which forms the flat wall and the textures. This immersed boundary can therefore be in close proximity to the bottom of the computational domain. See Strand (2007) for a detailed discussion of the locations, purposes and interactions of the various immersed boundaries in the domain.

2.3. Surfaces examined

A primary goal of this work was to investigate the growth and spreading of turbulent spots over surface textures that could be applied in a practical engineering situation. For this reason, triangular riblets were chosen.

The riblets simulated here are solid, no-slip surfaces created with the immersed boundary method. Since the body forces are applied at the grid nodes, the riblets are slightly stairstepped rather than completely smooth. If a sufficiently high resolution is used (so that each riblet is at least 5 or 6 grid nodes high) this stairstepping is not a problem. For more detail on how the various immersed boundaries are created, see Goldstein *et al.* (1995).

The riblets do not begin immediately downstream of the buffer zone, instead they begin at $0.311L$. (L is the total length of the domain in the streamwise direction. For reference, the buffer zone ends at $0.124L$.) This is done so that the buffer zone does not interact directly with the riblets. The riblets begin flush with the wall and ramp up to their full height over a distance of $0.06L$, reaching their full height at $0.374L$. The ramping is done so that the riblets do not themselves trip the boundary layer. The riblet height and crest-to-crest spacing are $1.06\delta_o^*$ and $1.11\delta_o^*$, respectively. These dimensions were chosen based on prior work (Strand 2007), in which, of the height

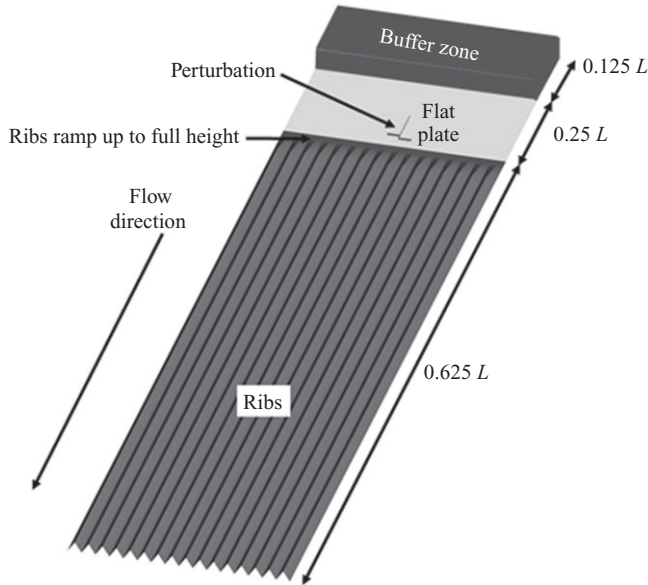


FIGURE 3. Schematic diagram for riblet case showing 16 riblets, the region of the perturbation and the buffer zone. L is the streamwise length of the domain.

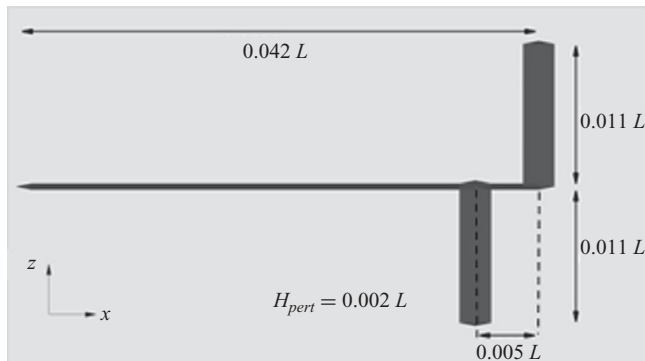


FIGURE 4. Perturbation shape used to generate the turbulent spots. Perturbation extends upward from the flat plate. H_{pert} is the perturbation height and L is the length of the domain in the streamwise direction.

and spacing combinations tested, they were the most successful at constraining spot growth.

Figure 3 is a schematic diagram of the riblet case. To improve the clarity of the schematic, the riblets used here have heights and spacings about three times that of the riblets used in the actual runs. Only the part of the domain near the bottom wall is shown; the suction wall is located well above the visible area.

2.4. Initial perturbation

The size and shape of the perturbation was determined by trial and error. As found by Wygnanski *et al.* (1976, 1982), if the flow is not perturbed strongly enough, no spot will develop. The perturbation used for the results presented in this report is shown in figure 4. It is a solid surface created with the same immersed boundary technique as the plate and the textures. The perturbation is located in the region

between the end of the buffer zone and the beginning of the riblets. The shape of the perturbation is set such that halving the grid in any direction does not alter its size or shape. It is made to appear at the beginning of the simulation, and is then removed after a brief time ($0.012T_{tot}$, where T_{tot} is the total length of the run). The perturbation is deliberately made asymmetric about the spanwise centreline in order to keep the spot from developing perfect left–right symmetry. Slight variations in the initial perturbation are used to generate differing spots over the same surface type (flat wall or riblets) for the purposes of ensemble-averaging (see below).

2.5. Ensemble-averaging

The growth and spreading of turbulent spots is a chaotic process and thus the detailed structure of a spot can be highly sensitive to small variations in the size and shape of the perturbation which triggers it. Past experimenters such as Wygnanski *et al.* (1976) used ensemble-averaging to generate the profile of a ‘typical’ spot. In the ensemble-averaging process, multiple spots are observed and results are averaged (the averaging method often takes into account the specifics of the experimental set-up) to determine the ensemble-averaged spot structure. In most (if not all) DNS studies of spots performed to date, however, the significant computational expense associated with simulating spots has prevented the use of ensemble-averaging.

When comparing textures to one another, it is especially important to separate changes in the spot growth caused by the textures from random variations in spot growth due to other factors. For example, the spot will grow at least slightly differently if the centroid of the perturbation is directly upstream of a riblet valley than it would if the centroid of the perturbation were directly upstream of a riblet crest. It is therefore difficult to ascertain the effects of riblets on spot growth by means of comparing a single spot over riblets with a single spot over a flat plate.

Within the limits of available computational resources, an attempt was made in this work to obtain ensemble-averaged spots over the flat plate and over the riblets. Four different spots were simulated for each case; the differences between the spots were the results of slight variations in the initial perturbation. Note that all figures in this paper which show flow structures are based on individual (as opposed to ensemble averaged) spots. For both the flat wall and the riblet cases, the spot which is generated by the first perturbation (shown in figure 4) is used for visualization. Ensemble averaging is only used for the calculation of spot half-width and spreading angle.

When examining the vortical structures inside spots, this work focuses on individual simulations, since ensemble-averaging would wash out these structures. The ensemble-averaging is used when determining the spreading angle, as discussed later.

3. Qualitative results

3.1. Flat-wall spot

Before the effects of riblets on spots are investigated, it is useful to examine spots over a flat plate. This provides a basis for comparison both with the riblet runs presented later and with the experiments, simulations and flow visualization found in the literature.

The domain used for these simulations had dimensions of $530.7\delta_o^*$, $21.2\delta_o^*$ and $106.1\delta_o^*$ in the streamwise (x), wall-normal (y) and spanwise (z) directions, respectively, where δ_o^* is the boundary-layer displacement thickness at the location of the perturbation, as calculated from the Blasius solution. For this domain, $512 \times 256 \times 512$ spectral modes were used in the x -, y - and z -directions, respectively. The perturbation

was introduced at $t=0$ and remained in the flow until $t=4.8\delta_o^*/U_\infty$. The simulation continued until $t=530.7\delta_o^*/U_\infty$, by which time the front tip of the spot had reached the end of the streamwise domain (and entered the buffer zone). The Reynolds number based on displacement thickness, Re_{δ^*} , was 376.8 at the perturbation location. Re_x at the end of the streamwise domain was $\sim 200\,000$.

A top-down view of the flat-wall spot at three equally spaced time intervals is shown in the top image of figure 5. As the spot matures, it takes on the expected arrowhead shape. It is asymmetric about the spanwise centreline since the perturbation itself is asymmetric. This was done intentionally, since experimental spots do not have perfect left/right symmetry. Perfect symmetry leads to some unrealistic results, such as values of zero on the spot centreline for the normal and streamwise vorticity, spanwise velocity and helicity. A quick glance at the figure indicates that the leading edge is moving at a fairly constant speed, since the leading edge moves about the same distance between t_1 and t_2 as it does between t_2 and t_3 .

The top image in figure 6 shows a close-up of the flat-wall spot at time t_3 from figure 5, this time using two isosurfaces of λ_2 , which is useful for picking out vortex cores (Jeong & Hussain 1995). Note the long streamwise vortical structures, especially near the edge of the spot. In this figure, the relaminarization of the flow after the passage of the spot is apparent, since there are no vortical structures present in the wake of the spot. Figure 7 is a flow visualization photograph of a turbulent spot in water, with $Re_x=200\,000$ in the centre of the spot (as compared to 150 000 for the spot shown in figure 6). The two spots are similar in shape, especially near the wingtips and at the rear, where long streamwise structures are clearly visible in both. The front tip of the spot is slightly sharper in figure 7, most likely because Re_x is somewhat higher for that spot, and spots tend to be more clearly defined at higher Re_x . This can be seen in several other flow visualization pictures from Van Dyke (1982), the source of figure 7.

Figure 8 shows a close-up side view of the flat-wall spot from figure 6. The overhang found by prior experiments and DNS is clearly visible near the leading edge of the spot. Note also that the spot remains significantly below the suction wall, and thus the body forces imposed by the suction wall are unlikely to affect the spot directly.

Schubauer & Klebanoff (1956) argued that the height of the spot can be estimated by the thickness of a hypothetical turbulent boundary layer which originates at the location of the perturbation, and which has an initial thickness equal to that of the laminar boundary layer at the perturbation ($\delta_{lam,pert}$). The data of Wignanski *et al.* (1982) also support this idea. In figure 9, isosurfaces of $|\omega_x|$ at the value of $0.188U_\infty/\delta_o^*$ are shown for several output time intervals simultaneously. The point is to see the variation in the peak height of the spot as it moves downstream. The hypothetical turbulent boundary-layer thickness, shown in the figure as well, is calculated from

$$\delta_{turb,hypothetical} = \frac{0.16(x - x_{pert})^{6/7} \nu^{1/7}}{U_\infty^{1/7}} + \delta_{lam,pert}, \quad (3.1)$$

where x_{pert} is the streamwise location of the perturbation, U_∞ is the free-stream velocity, and ν is the kinematic viscosity. The one-seventh power-law expression was used to describe the growth of the turbulent boundary layer (White 1991). It is apparent from the figure that the height of the flat-wall spot fits this approximation fairly well. This is a further indication that the suction wall is not having direct effects on the growth of the spot and that the spot is growing properly as it moves downstream.

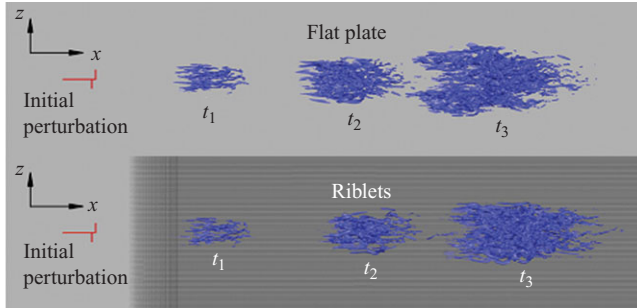


FIGURE 5. Top view of a turbulent spot over a flat wall and riblets (top and bottom images, respectively), drawn with isosurfaces of $|\omega_x|$ at the value of $0.188U_\infty/\delta_o^*$ and shown at $t_1 = 127.4\delta_o^*/U_\infty$, $t_2 = 276.0\delta_o^*/U_\infty$ and $t_3 = 424.6\delta_o^*/U_\infty$. Each image shows streamwise domain from $16.3\delta_o^*$ to $447.9\delta_o^*$ downstream of the buffer zone. Full spanwise domain is shown.

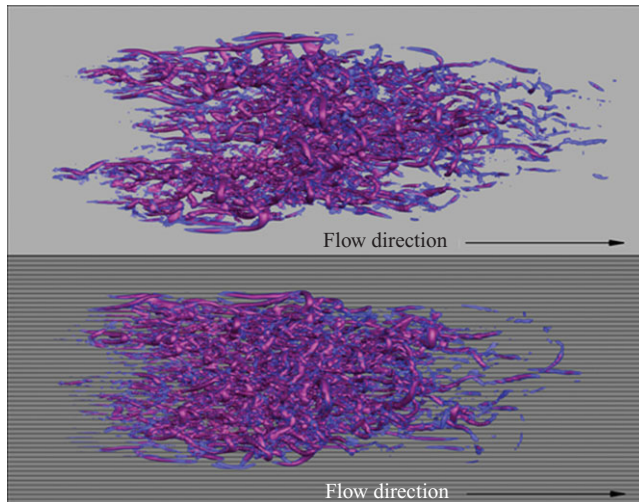


FIGURE 6. Close-ups of turbulent spots over a flat wall and riblets (top and bottom images, respectively), drawn with isosurfaces of λ_2 at the values of $-0.0044(U_\infty/\delta_o^*)^2$ and $-0.0089(U_\infty/\delta_o^*)^2$ (with the first isosurface being translucent). Spots are shown at $t = 424.6\delta_o^*/U_\infty$. Top and bottom images show streamwise domain from $271.1\delta_o^*$ to $424.1\delta_o^*$ and $294.5\delta_o^*$ to $448.4\delta_o^*$ downstream of the buffer zone, respectively. Both images show spanwise domain from $24.2\delta_o^*$ from the left edge of the domain to $82.8\delta_o^*$ from the right edge of the domain.

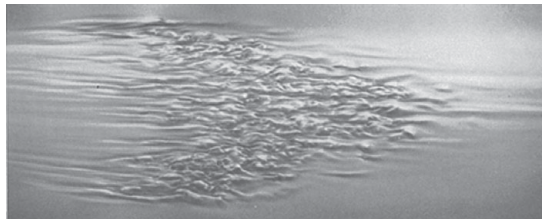


FIGURE 7. Top-down view of a turbulent spot over a flat plate, visualized with aluminium flakes in water. Image by Cantwell, Coles & Dimotakis (1978), taken from *An Album of Fluid Motion*, by Milton Van Dyke (1982), reproduced by kind permission. $Re_x = 200\,000$ in the centre of the spot.

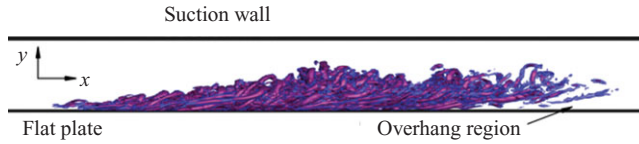


FIGURE 8. Side view of the spot in figure 6, at the same time, and shown with the same isosurfaces. Streamwise domain is the same as that shown in the top image of figure 6. Suction wall is located $17.0\delta_o^*$ above the flat plate.

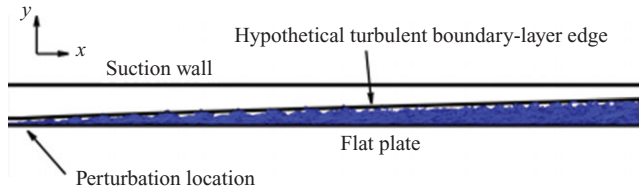


FIGURE 9. Comparison of the spot height with the thickness of a hypothetical turbulent boundary layer originating at the perturbation, with an initial height equal to the laminar boundary-layer thickness at the perturbation. Streamwise domain is shown from $66.3\delta_o^*$ to $447.9\delta_o^*$ downstream of the buffer zone. Suction wall is located $17.0\delta_o^*$ above the flat plate.

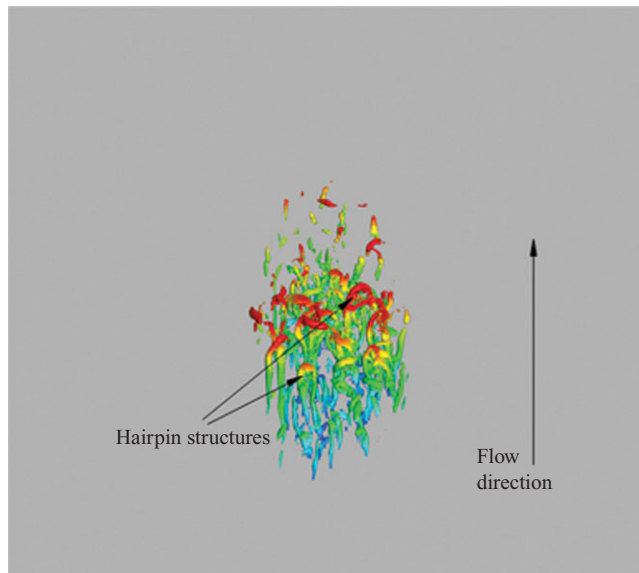


FIGURE 10. Perspective view from the top rear of the flat-wall spot at time $t = 212.3\delta_o^*/U_\infty$ shown with an isosurface of λ_2 at the value of $-0.0089(U_\infty/\delta_o^*)^2$, coloured by contours of the wall-normal coordinate. Viewer is 40° above the horizontal looking down towards the spot and facing downstream. Hairpins appear to be reasonably similar in size. The figure shows streamwise domain from $153.3\delta_o^*$ to $296.7\delta_o^*$ downstream of the buffer zone. Full spanwise domain is shown.

Figures 10–12 are oblique perspective views from the rear of the spot at different times. In these figures, a single isosurface of λ_2 is present, at the value of $-0.0089(U_\infty/\delta_o^*)^2$. This isosurface is coloured by contours of the wall-normal (y) coordinate in order to distinguish between the heads and the legs of the hairpin vortices. The usefulness of λ_2 is apparent here; these isosurfaces clearly display the

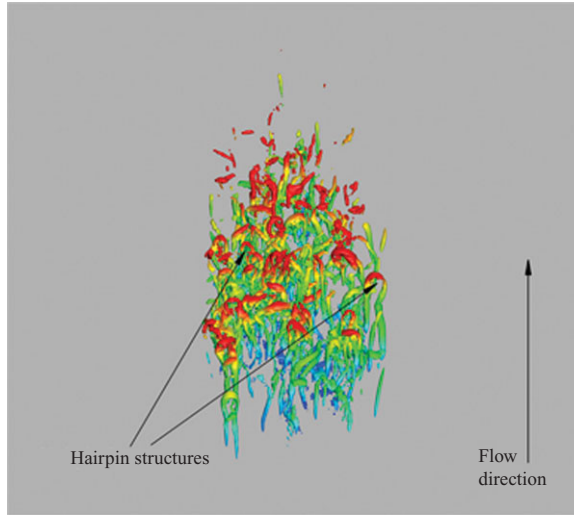


FIGURE 11. Perspective view from the top rear of the flat-wall spot at time $t = 318.4\delta_0^*/U_\infty$ shown in the same way as the spot in figure 10. The range of hairpin sizes appears to be increasing. The figure shows streamwise domain from $215.9\delta_0^*$ to $359.3\delta_0^*$ downstream of the buffer zone. Full spanwise domain is shown.

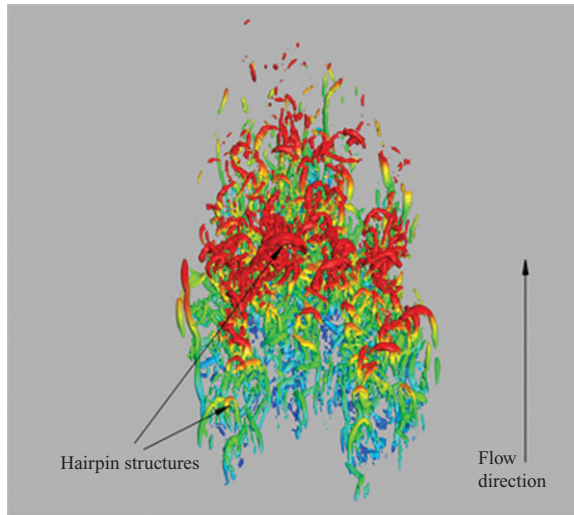


FIGURE 12. Perspective view from the top rear of the flat-wall spot at time $t = 424.6\delta_0^*/U_\infty$, shown in the same way as the spot in figure 10. A wide variety of hairpin scales are apparent. The figure shows streamwise domain from $280.7\delta_0^*$ to $425.1\delta_0^*$ downstream of the buffer zone. Full spanwise domain is shown.

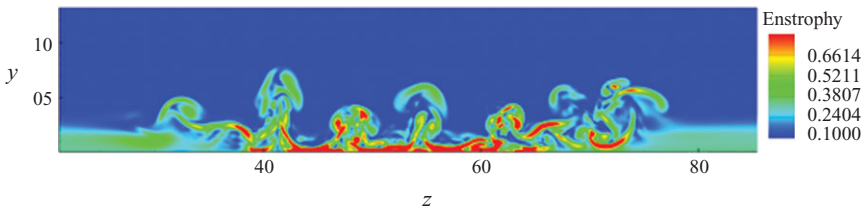


FIGURE 13. Contours of enstrophy on a z - y plane located $392.6\delta_0^*$ downstream of the perturbation, at time $t = 424.6\delta_0^*/U_\infty$. The units of enstrophy are U_∞/δ_0^* .



FIGURE 14. Cross-section of a turbulent spot over a flat plate in a wind tunnel. Smoke is used to visualize the spot. Image by Perry, Lim & Teh (1981), taken from *An Album of Fluid Motion*, by Milton Van Dyke (1982).

multiple overlapping and entwined hairpin and streamwise vortical structures that make up the spot. Hairpins are present throughout the spot in all three figures. The structures are more complex and intertwined in the spot centre, and the hairpin legs do not necessarily align fully with the streamwise direction. The hairpins present in the first image (figure 10) are almost all of roughly the same size. As the spot matures the range of hairpin sizes increases, and in the last image (figure 12) a wide variety of hairpin scales is apparent. This increasing range of hairpin scales is consistent with the fact that the spot is becoming more fully developed as it grows and propagates downstream. Just as the range of scales in a turbulent boundary layer increases along the length of a flat plate (White 1991), it would be reasonable to guess that the range of scales of the vortical structures within a turbulent spot would increase as the spot matures, and figures 10–12 appear to confirm this idea.

Near the spot wingtips, both hairpins and other streamwise vortices are present. These other streamwise vortex structures appear to be the ‘quasi-streamwise vortices’ described by Singer (1996). However, in the light of these figures it is likely that these quasi-streamwise vortices are simply the outside legs of hairpins whose heads are just inside the spot edge.

Figure 13 is a cross-section (a zy slice) of the flat-wall spot displaying contours of enstrophy. Note that the regions of greatest enstrophy are mostly concentrated near the wall. The prominent mushroom-like structures are created when fluid erupts away from the wall due to the interaction of hairpin vortex structures with each other and with the wall. It is apparent from figure 13 that there is not a large region of semi-turbulent flow at the edges of the spot. The edges are relatively sharp, with a quick jump from turbulent to laminar flow. The topic of defining the spot edges is discussed in the section on spreading angle.

Figure 14 is a photograph showing a cross-section of a spot over a flat plate in a wind tunnel, where smoke is used to visualize the spot. The same mushroom-like structures that are seen in figure 13 are also clearly visible here, and the ratio of spot width to spot height appears approximately the same in this instance.

It is worthwhile to calculate the friction length scale, l^* , for the turbulent spot. For an incompressible, constant viscosity fluid, l^* is a function only of the velocity gradient at the wall:

$$l^* = \sqrt{\frac{\nu}{\left. \frac{du}{dy} \right|_{wall}}}. \quad (3.2)$$

This velocity gradient can be calculated in post-processing in order to obtain values of l^* for the simulated spots. The spot simulations are three-dimensional, and therefore in the region in and around the spot every (x, z) location will have a different value of l^* . The friction length scale can also be calculated for a Blasius boundary layer. In

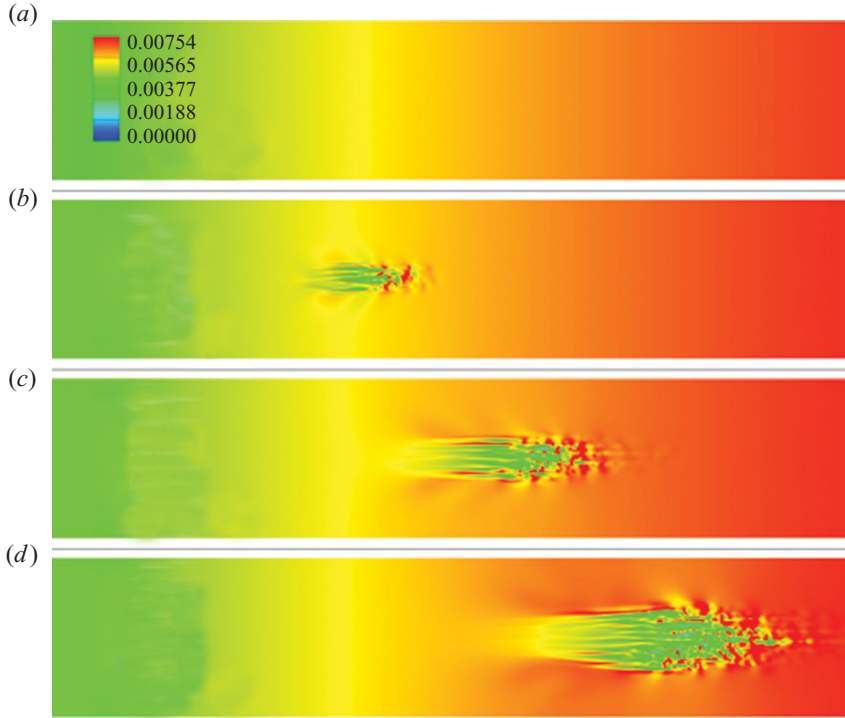


FIGURE 15. Contours of l^* (units of δ_o^*) (a) for a Blasius boundary layer and (b–d) for a turbulent spot over a flat plate at $t = 223.5\delta_o^*/U_\infty$, $t = 351.2\delta_o^*/U_\infty$ and $t = 479.08\delta_o^*/U_\infty$, respectively. Each image shows all of the streamwise domain past the end of the buffer zone. Full spanwise domain is shown.

that case,

$$l^* = (1.7354) \frac{\nu^{3/4} x^{1/4}}{U_\infty^{3/4}}, \quad (3.3)$$

where 1.7354 is a numerical factor coming from the Blasius solution. The Blasius solution is two-dimensional, and thus l^* varies only with streamwise location along the plate.

Figure 15 shows contours of the Blasius value for l^* , along with l^* calculated from the simulation results for a spot over a flat plate at several levels of development. The values of l^* in regions well outside the spot agree with the analytical Blasius value. Within the spot, l^* is appreciably smaller than the Blasius value. At all three stages of the spot's development, the l^* contours are remarkably similar. The calm but non-Blasius region to the rear of the spot is evident in these images. In the bulk of the spot, l^* is lower than the Blasius value, indicating that the velocity gradient at the wall is higher. This is not surprising, since the flow field in the centre of the spot is similar to that in a turbulent boundary layer, and $du/dy|_{wall}$ is higher for a turbulent boundary layer than for a laminar boundary layer at the same U_∞ and streamwise location. The average value of l^* within the spot changes very little as the spot moves downstream. The value of l^* in the surrounding laminar boundary layer changes significantly and the spot more than doubles in size between the earliest and latest images in figure 15, but the interior of the spot is dominated by the same green

contour level in both. In a turbulent boundary layer, l^* is inversely proportional to $x^{1/14}$ (derived from equations in White 1991, pp. 429–430). It was shown previously that spot growth in the wall-normal direction is well described by the one-seventh power law that describes turbulent boundary-layer growth. Thus, it is reasonable to expect that the variation with distance along the plate of l^* within the spot will be similar to the variation of l^* with streamwise location in a fully turbulent boundary layer. With this in mind, even though Re_x doubles, l^* would only be expected to grow by 5%.

Estimating from these images, the value of l^* in the interior of the spot is approximately $0.05\delta_o^*$. If it is assumed that, for a spot over the type of riblets examined in this work, l^* is roughly equivalent to l^* for a spot over a flat plate, then it is possible to calculate h^+ and s^+ (h^+ = riblet height/ l^* and s^+ = riblet crest-to-crest spacing/ l^*). The riblet height and spacing are $1.06\delta_o^*$ and $1.11\delta_o^*$, respectively, so for the riblets used in this work, $h^+ \approx 21$ and $s^+ \approx 22$. These s^+ values are within the range for which riblets were found to reduce drag in a fully turbulent boundary layer (Bruse *et al.* 1993). However, Bruse *et al.* (1993) found that at this value of s^+ , riblets with $h/s \approx 1$ (such as those used in this work) actually increased the drag (as opposed to riblets with $h/s \approx 0.5$ or $h/s \approx 0.7$, both of which reduced drag for this value of s^+).

Having an approximate value for l^* also provides insight concerning grid resolution. Using the value of $l^* \approx 0.05\delta_o^*$ found from figure 15, the grid resolution in the streamwise direction is found to be $\Delta x/l^* \approx 20$, while in the spanwise direction it is $\Delta z/l^* \approx 4$. In the wall-normal direction, the grid spacing is not constant, but for the grid cell just above the plate the resolution is $\Delta y/l^* \approx 0.08$ and the highest value of $\Delta y/l^*$ in the domain is ~ 2.6 . These values are all similar to those used by Goldstein & Tuan (1998), who demonstrated grid convergence at these resolutions in a fully turbulent channel flow with and without riblets.

3.2. Riblets

The domain, grid and perturbation for the riblet case are the same as those for the flat-wall case. As mentioned earlier, the riblet height and spacing are $1.06\delta_o^*$ and $1.11\delta_o^*$, respectively. There are a total of 96 riblets across the spanwise extent of the domain.

Figure 5(bottom) shows results for the turbulent spot over riblets (compared with the flat-wall case in figure 5(top), as discussed earlier). It is apparent from the figure that the textures do not dramatically reduce spot growth. The overall arrowhead shape of the spot is largely maintained and the front tip velocity of the spot is not altered significantly by the riblets.

Figure 6(bottom) shows a close-up top-down view of the spot for the riblet case. When compared with the flat-wall case in figure 6(top), as discussed earlier, there is not a great deal of qualitative difference between the spots. Both have the same intertwined hairpin structures and roughly the same density of vortical structures inside the spot (neither of the cases has clearly weaker or stronger turbulence inside the spot than the other).

4. Quantitative measures of spot growth and spreading

4.1. Defining the spot

There are several ways to define the boundaries of a turbulent spot. Most often, the spot boundaries are defined by a cutoff value for some specific flow variable. If the value of the variable is greater than the cutoff value in a specific region, then that

region is defined to be part of the spot, otherwise it is considered outside the spot. Since one of the primary goals of this work is to investigate how the spreading of a spot is affected by surface textures, a consistent and precise definition of the spot edge or boundary is important. Several factors influenced the decision on how to define the spot. First, the chosen variable should have values near zero in a laminar, flat-plate boundary layer. Even when textures are introduced, in the laminar case the values of this variable should be small throughout the majority of the domain. At the same time, its values should become quite large (relative to the laminar case) inside the spot, so that it is useful for picking out the spot from the background flow. This is especially important in the presence of surface textures, since many quantities that could normally be used to define the spot (such as enstrophy, vertical velocity and the vertical component of vorticity) become large not only inside the spot but also along the crests of the textures. When examining so many different spots, at so many different time steps, it is impossible to accurately ‘eyeball’ the output to determine the edge of the spot. It is necessary to determine the spreading angle in an automated way. Thus, it is essential that the chosen quantities pick out the spot from the textures without the need for qualitative examination in every case. The above considerations resulted in the choice of the magnitude of the streamwise component of vorticity, $|\omega_x|$, as the variable which will define the spot.

The output from each run includes the three-dimensional flow field at 30 different times (with an interval of $21.2\delta_o^*/U_\infty$ between each output time). At each output time, the location of the ‘right’ and ‘left’ lateral edges of the spot is determined. Right and left are from the perspective of an observer looking downstream. The spot edge (for either the right or left side) is defined as the point on the spot which is farthest from the spot centreline (a straight line which is drawn from the centroid of the perturbation, parallel to the free-stream direction). The spot edge on each side is calculated with four different cutoff values of $|\omega_x|$. The cutoff values of $|\omega_x|$ are $0.141U_\infty/\delta_o^*$, $0.188U_\infty/\delta_o^*$, $0.235U_\infty/\delta_o^*$ and $0.282U_\infty/\delta_o^*$. These four values are averaged to give one location for the spot edge on each side, and then the left and right edge locations are averaged to obtain one overall edge location. Thus, at every time interval, the final spot edge location is the average of eight values (the right edge location defined with four cutoff values of $|\omega_x|$, and the left edge defined with the same four cutoff values). Note that average values are computed for both the distance from the centreline to the spanwise edge of the spot (the spot half-width) and for the streamwise location of the spot edge.

Finally, an ensemble-averaged edge location at each time interval is obtained from the four spots which were run for each surface type. The edge location at each time interval is simply the arithmetic average of the edge locations of the four individual spots. It is this ensemble-averaged edge location which is used to define the spreading angle for the spot over each surface type.

4.2. Defining the spreading angle

Even after defining the edges of the spot, it is still not completely clear what is meant by the ‘spreading angle’. The key distinction is whether the spreading angle is measured from the perturbation or from a virtual origin. Figure 16 illustrates the difference.

Several spots were examined to determine whether or not a virtual origin is appropriate. In figure 17, the ensemble-averaged spot half-width is plotted against the ensemble-averaged streamwise location of the spot edge for the flat-wall spot. Two distinct growth regimes are present, indicating that a virtual origin should be used for

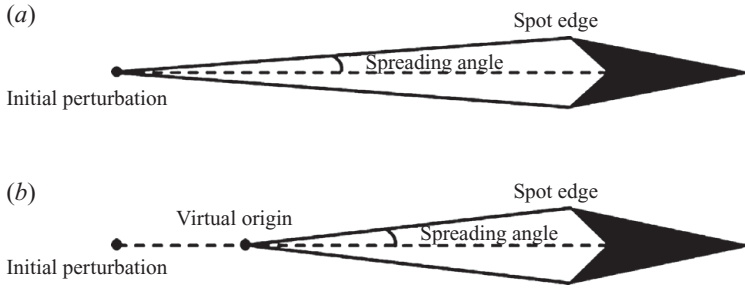


FIGURE 16. Spreading angle measured from the initial perturbation (a) and from a virtual origin downstream of the initial perturbation (b).

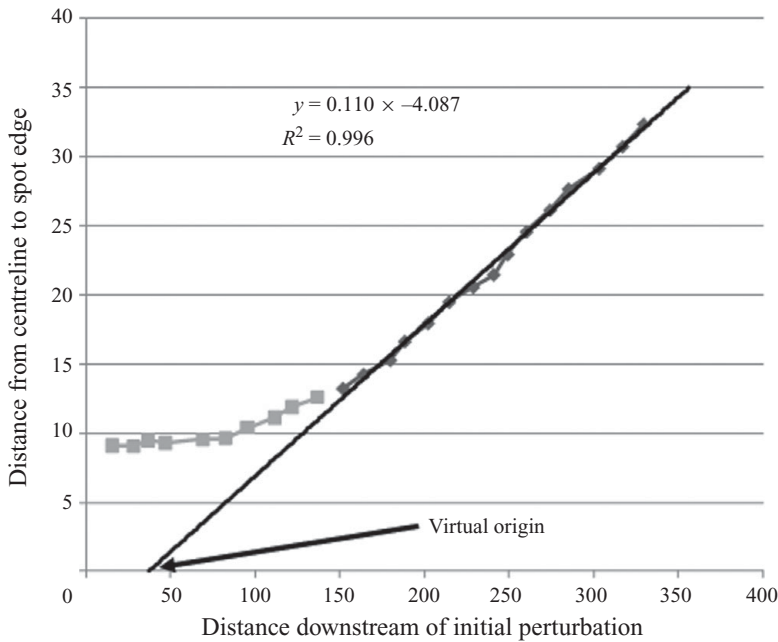


FIGURE 17. Growth of the ensemble-averaged spot over a flat plate. Note the nonlinear early growth of the pre-turbulent spot (shown by light grey) and the linear growth of the developed spot (shown by dark grey). The linearity of this growth is indicated by the high R^2 value for the linear trend line (shown by black). Both axes are in units of δ_o^* .

the spreading angle. In the region just downstream of the perturbation, the growth of the very young spot does not follow a linear pattern. Further downstream the growth rate takes on a reasonably constant value, and in this region a line can be fit through the spot edge locations, as seen in figure 17. Using linear regression to calculate the equation for this line, the location of the virtual origin and the spreading angle can be easily determined. In this case, the spreading angle is 6.3° and the virtual origin is located $37.3\delta_o^*$ downstream of the initial perturbation.

4.3. Spreading angle results

The method described above was used to calculate the spreading angle for the ensemble-averaged spots over the flat plate and riblets. The spreading angle for the spot over the flat wall was 6.3° while the spreading angle for the spot over riblets was

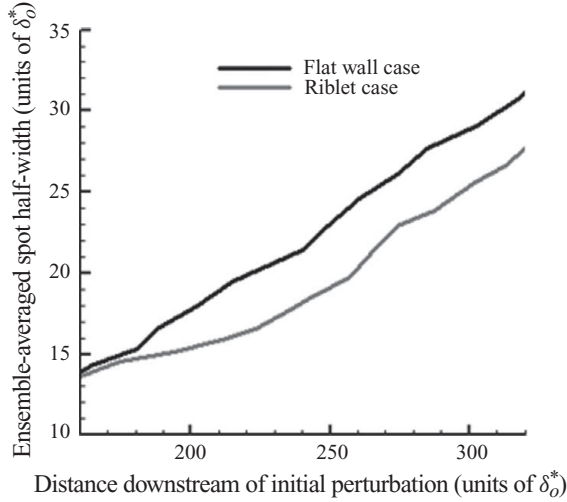


FIGURE 18. Growth of ensemble-averaged spots over a flat plate and riblets.

5.4°. The flat-wall spreading angle of 6.3° is very close to the 6.4° reported by Singer (1996) and also reasonably close to the 7° spreading angle reported by Henningson *et al.* (1987) for the ‘turbulent vortical region’ of a spot. The difference between this spreading angle and the commonly quoted experimental value of 10° most likely arises partly due to the method of defining spreading angle. The fact that the spots simulated in this work are at a significantly lower Reynolds number than that used in most experiments ($\sim 200\,000$ as compared with 600 000 for the experiments of Wygnanski *et al.* 1976) also explains some of the difference.

The spreading angle for the spot over riblets is 5.4°, a decrease of 14 % compared to the flat-wall case. This is in reasonable agreement with the results presented by Strand (2007). This decrease in spreading is not an artefact of the least-squares linear regression or some other aspect of the method of calculation. The decrease in spreading can easily be seen by comparing plots of spot half-width versus distance downstream of the initial perturbation for the flat-wall and riblet cases, as shown in figure 18.

5. Conclusions

Several conclusions can be drawn from the work presented here. First, it is possible with the suction wall method to simulate a boundary layer spot with a spectral DNS code originally designed for channel flow. It is also possible to use the immersed boundary method to simulate spot growth over a flat plate and textured surfaces.

Perhaps the most important conclusion of this work is that turbulent spots are composed of a multitude of entwined hairpin vortices. This is in agreement with the results of Krishnan & Sandham (2007) and Jocksch & Kleiser (2008) for turbulent spots in compressible flows and the preliminary results of Strand (2007) and Strand & Goldstein (2010). Furthermore, it has been shown here that the range of scales of the hairpin vortices increases as the spot matures.

Concerning the goal of constraining spot growth, the present results are mixed. The riblets decreased the spreading angle by 14 %, which is not enough to significantly delay the onset of full turbulence. However, these riblets have not been fully optimized.

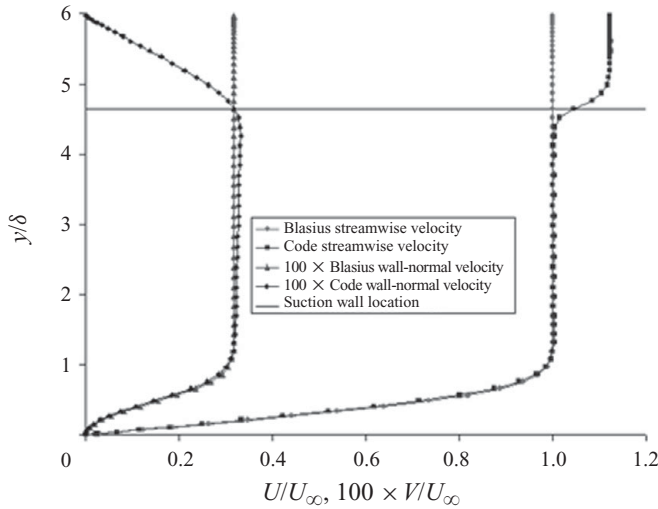


FIGURE 19. Comparison of the boundary-layer profile developed with the suction wall method to that predicted by the Blasius solution midway down the plate. Note that the simulated vertical velocity agrees with the Blasius value at the suction wall location.

Their height and spacing were chosen based on the best case out of the limited number tried in prior work; however, many other height and spacing combinations might be tried. Other shapes could also be tried, such as cusped or sawtooth riblets. Furthermore, in the current work the textures maintain their height and spacing along the entire length of the domain, even as the turbulent spot increases greatly in size. It is possible that the height and/or spacing of optimum textures may be a function of streamwise location along the plate. For example, figure 18 appears to show a stronger effect of riblets at lower Re_x , suggesting that optimized riblets might have to grow with downstream distance. Finally, recent work with riblets placed at an angle with respect to the streamwise direction has shown promise (Chu *et al.* 2010).

This work was sponsored by AFOSR through grant FA 9550-08-1-0453.

Appendix

A.1. Blasius profile verification

It was necessary to verify that the suction wall method permitted proper spatial development of the boundary layer, so profiles were examined for several downstream locations and compared with the Blasius solution. Figure 19 shows the boundary-layer profile at the midpoint of the domain over a flat wall. The profile corresponds to a position along the plate which is 54.57δ from the leading edge, where δ is the boundary layer 99% thickness at the streamwise location of the profile shown. The flow is completely uniform in the spanwise direction. Both the streamwise and wall-normal velocity components are shown in the figure, and both compare well with the Blasius solution.

A.2. Grid convergence

It is very difficult to establish grid convergence for these types of simulations. The growth of a turbulent spot is a chaotic process, and thus the final detailed structure of

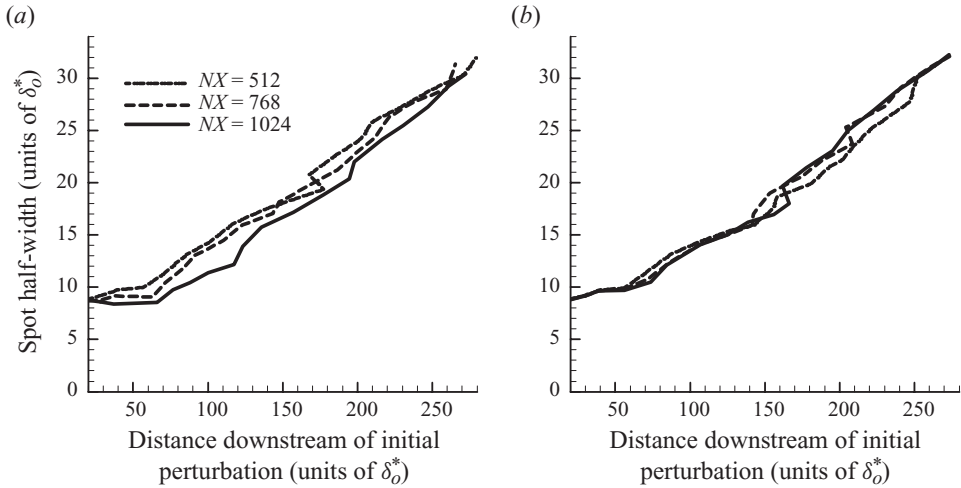


FIGURE 20. Growth of spots over a flat plate at various resolutions. (a) Streamwise direction grid resolution study, (b) spanwise direction grid resolution study. Resolution is $NY = 64$, $NZ = 512$ for all three cases in (a) and $NY = 64$, $NX = 512$ for all three cases in (b). Note that these are single spots, not ensemble-averaged results.

the spot is highly sensitive to the initial perturbation and to the exact texture shapes. Even in the case of spots over a flat wall, tiny differences in the eddy structure between two similar spots will grow chaotically over time, and after the spots have propagated a significant distance downstream they will appear completely different at the finest scales.

The body forces that create the immersed boundaries (flat plate, textures, perturbation, buffer zone and suction wall) are applied at the grid nodes. Even if the grid resolution is more than adequate to model the flow field, simulations with different resolutions will still have differences in the body force field which is applied to generate the textures. Thus, even with vast computational resources, it would be nearly impossible to demonstrate grid convergence by comparing the exact eddy structure within spots simulated with different grid resolutions.

In order to study grid convergence in a more quantitative way, it is necessary to define a quantity of interest (QoI) so that we may examine grid convergence with respect to this specific quantity, rather than in a general, qualitative sense. One quantity of interest which is relevant to this work is the half-width of a turbulent spot, as defined earlier in the section on spreading angle.

Because of computation time and memory constraints, it was not possible to significantly increase the grid resolution in any direction while holding the others constant. Therefore, grid convergence was examined in two parts. The first part focused on the streamwise (x) and spanwise (z) directions. For these convergence runs, the wall-normal resolution was lowered to 64 (as opposed to 256 for the runs presented earlier in this work). This is the wall-normal resolution used in our previous work (Strand 2007). Although it may be too low for quantitative comparisons between spots over the flat wall and textures, it is sufficient to examine the grid convergence trends in the other two directions.

Figure 20 shows plots of spot half-width (our QoI) versus distance downstream of the initial perturbation for the flat-wall spot with various resolutions ($NY = 64$, $NZ = 512$ for all three cases in figure 20a and $NY = 64$, $NX = 512$ for all three cases

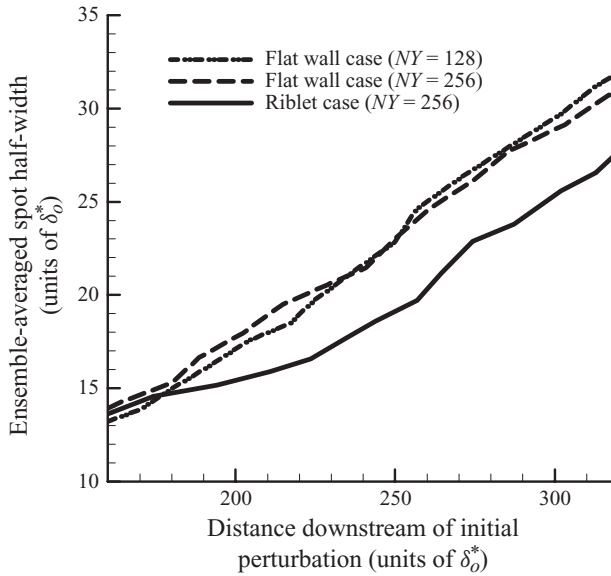


FIGURE 21. Growth of ensemble-averaged spots over a flat plate (at two different wall-normal resolutions) and over riblets. Resolution is $NX = 512$, $NZ = 512$ for all three cases.

in figure 20*b*). In both images, the growth of the spot does not appear to be greatly affected by the grid resolution. Note that due to computational time constraints these runs were not ensemble-averaged.

The second part of the grid convergence study focused on the grid resolution in the wall-normal (y) direction. The wall-normal grid resolution used in prior work (Strand 2007) was considered inadequate, and therefore in this work the wall-normal resolution was quadrupled (from $NY = 64$ to $NY = 256$). Computational constraints prevented significantly increasing the grid in the wall-normal direction beyond $NY = 256$, so instead a second set of flat-wall cases was run with $NY = 128$, which is half the resolution used in the rest of the paper. These cases were ensemble-averaged in the same way as the normal flat-wall cases, and the results are shown in figure 21. Also shown in figure 21 is the ensemble-averaged riblet case from this work. It is clear from the figure that the differences between the two flat-wall cases are minor compared with those between the flat-wall case and the riblet case. This figure provides strong evidence that the effects of riblets on spots which were discussed earlier are genuine, and not an anomaly due to grid resolution.

A.3. Channel height and pressure gradient effects

As a test, a spot was allowed to develop over a flat wall with the suction wall turned off. With the suction wall off, a favourable pressure gradient exists in the streamwise direction, as discussed previously. Katz, Seifert & Wygnanski (1995) found that a strong favourable pressure gradient dramatically reduces spot growth. The pressure gradient which develops in this case is not as strong as that used by Katz *et al.* (1995), but the spreading angle is nonetheless reduced by 25% compared with the ensemble-averaged flat-wall value.

This test was performed because in the simulations presented here a very small favourable pressure gradient develops in the channel, with the suction wall on. This occurs for two reasons. First, in all of the cases, once the spot begins to grow, $d\delta^*/dx$

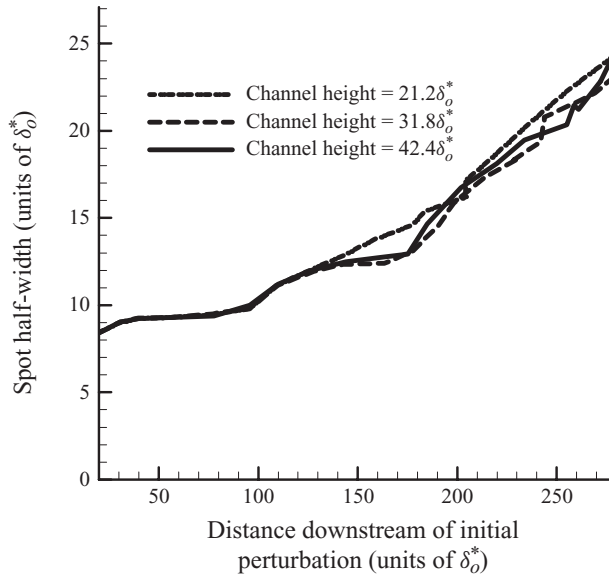


FIGURE 22. Growth of spots over a flat plate for computational domains with three different channel heights.

increases in the region in and around the spot, and thus more fluid is pushed up towards the suction wall. The suction wall flow rate is based on the analytical solution for a Blasius profile. Thus, a slight favourable pressure gradient develops. Second, in the cases with surface textures, $d\delta^*/dx$ jumps above the flat-wall value in the region where the textures ramp up to full height. This leads to a jump in the boundary-layer edge velocity (U_{edge}) in this region, but U_{edge} remains essentially constant throughout the rest of the domain after this jump.

Both of these effects decrease in importance as the channel height increases relative to the boundary layer height. If the channel height was allowed to grow very large compared with the boundary-layer thickness, the pressure gradient would eventually become negligible.

It was also considered a possibility that the proximity of the suction wall to the top of the spot might affect its growth, and that spots would therefore grow differently depending on the channel height. This would be unacceptable, since the channel height has no physical meaning for a boundary-layer simulation, it is purely a computational parameter.

In order to determine whether the channel height affects the spot growth, three flat-wall spots were simulated, one with the normal channel height used in all the other runs in this work, one with a 50% taller channel, and another with a 100% taller channel. These simulations were performed prior to the other runs presented here, and the wall-normal resolution used for them was slightly lower ($NY = 192$ as opposed to $NY = 256$). However, based on the grid convergence results above, that resolution should be sufficient. Plots of spot half-width versus distance downstream of the perturbation are shown in figure 22 for the three channel heights. The results are very similar in all three cases, especially considering that these spots are not ensemble-averaged. There is nothing in the figure which indicates that channel height has any significant effect on spot growth (as long as the channel is large enough so

that the top of the spot remains well below the suction wall at all times, which is the case in all of the simulations presented in this work).

REFERENCES

- AMINI, J. & LESPINARD, G. 1982 Experimental study of an ‘insipient spot’ in a transitional boundary layer. *Phys. Fluids* **25** (10), 1743–1750.
- BREUER, K. S. & LANDAHL, M. T. 1990 The evolution of a localized disturbance in a laminar boundary layer. Part 2. Strong disturbances. *J. Fluid Mech.* **220**, 595–621.
- BRUSE, M., BECHERT, D. W., TH. VAN DER HOEVEN, J. G., HAGE, W. & HOPPE, G. 1993 Experiments with conventional and with novel adjustable drag-reducing surfaces. In *Near-wall Turbulent Flows: Proceedings of the International Conference*, pp. 719–738. Tempe, AZ.
- CANTWELL, B., COLES, D. & DIMOTAKIS, P. 1978 Structure and entrainment in the plane of symmetry of a turbulent spot. *J. Fluid Mech.* **87**, 641–672.
- CHU, J., STRAND, J. & GOLDSTEIN, D. 2010 Investigation of turbulent spot spreading mechanism. In *48th AIAA Aerospace Sciences Meeting, Orlando, Florida. AIAA Paper* 2010-0716.
- COLMENERO, G. E. 2004 Turbulent boundary layer control with discrete actuators using wall information. Master’s thesis, Aerospace Engineering Department, The University of Texas at Austin.
- COUSTOLS, E. & SAVILL, A. M. 1992 Turbulent skin-friction drag reduction by active and passive means. Parts 1 and 2. Special course on skin-friction drag reduction. *AGARD Rep.* 768, pp 1–8 to 8–55.
- ELDER, J. W. 1960 An experimental investigation of turbulent spots and breakdown to turbulence. *J. Fluid Mech.* **9**, 235–246.
- EMMONS, H. W. 1951 The laminar–turbulent transition in a boundary layer. Part I. *J. Aeronaut. Sci.* **18** (7), 490–498.
- GOLDSTEIN, D. B., COHEN, J. & LEVINSKI, V. 2001 DNS of hairpin vortex formation in Poiseuille flow due to two-hole suction. In *The Third AFOSR International Conference on DNS and LES, Arlington, TX*.
- GOLDSTEIN, D. B., HANDLER, R. & SIROVICH, L. 1993 Modeling a no-slip flow boundary with an external force field. *J. Comput. Phys.* **105**, 354–366.
- GOLDSTEIN, D. B., HANDLER, R. & SIROVICH, L. 1995 Direct numerical simulation of turbulent flow over a modeled riblet covered surface. *J. Fluid Mech.* **302** (10), 333–376.
- GOLDSTEIN, D. B. & TUAN, T.-C. 1998 Secondary flow induced by riblets. *J. Fluid Mech.* **363**, 115–151.
- HANDLER, R. A., HENDRICKS, E. W. & LEIGHTON, R. I. 1989 Low Reynolds number calculation of turbulent channel flow: a general discussion. *NRL Mem. Rep.* 6410, pp. 1–103.
- HENNINGSON, D., SPALART, P. & KIM, J. 1987 Numerical simulations of turbulent spots in plane Poiseuille and boundary layer flow. *Phys. Fluids* **30**(10), 2914–2917.
- JEONG, J. & HUSSAIN, F. 1995 On the identification of a vortex. *J. Fluid Mech.* **285**, 69–94.
- JOCKSCH, A. & KLEISER, L. 2008 Growth of turbulent spots in high-speed boundary layers on a flat plate. *Intl J. Heat Fluid Flow* **29**, 1543–1557.
- KATZ, Y., SEIFERT, A. & WYGNANSKI, I. J. 1995 On turbulent spots in a laminar boundary layer subjected to a self-similar adverse pressure gradient. *J. Fluid Mech.* **296**, 185–209.
- KIM, J., MOIN, P. & MOSER, R. 1987 Turbulence statistics in fully developed channel flow at low Reynolds number. *J. Fluid Mech.* **177**, 133–166.
- KRISHNAN, L. & SANDHAM, N. D. 2007 Strong interaction of a turbulent spot with a shock-induced separation bubble. *Phys. Fluids* **19**, 016102.
- NARASIMHA, R. 1985 The laminar–turbulent transition zone in the boundary layer. *Prog. Aerosp. Sci.* **22** (1), 29–80.
- PERRY, A. E., LIM, T. T. & TEH, E. W. 1981 A visual study of turbulent spots. *J. Fluid Mech.* **104**, 387–405.
- SCHUBAUER, G. B. & KLEBANOFF, P. S. 1955 Contributions on the mechanics of boundary-layer transition. *NACA TN*-3489.
- SCHUBAUER, G. B. & KLEBANOFF, P. S. 1956 Contributions on the mechanics of boundary-layer transition. *NACA TR*-1289.
- SINGER, B. 1996 Characteristics of a young turbulent spot. *Phys. Fluids* **8** (2), 509–521.

- SINGER, B. & JOSLIN, R. 1994 Metamorphosis of a hairpin vortex into a young turbulent spot. *Phys. Fluids* **6** (11), 3724–3736.
- STRAND, J. 2007 DNS of surface textures to control the growth of turbulent spots. Master's thesis, The University of Texas at Austin.
- STRAND, J. & GOLDSTEIN, D. 2007 DNS of riblets to control the growth of turbulent spots. In *45th AIAA Aerospace Sciences Meeting, Reno, NV. AIAA Paper* 2007-1312.
- STRAND, J. & GOLDSTEIN, D. 2010 DNS of surface textures to control the growth of turbulent spots. In *48th AIAA Aerospace Sciences Meeting, Orlando, FL. AIAA Paper* 2010-0915.
- VAN DYKE, M. 1982 *An Album of Fluid Motion*. The Parabolic Press.
- WHITE, F. M. 1991 *Viscous Fluid Flow*, chap. 4, 2nd edn. McGraw Hill.
- WU, X. & MOIN, P. 2008 Direct numerical simulation of turbulence in a nominally zero-pressure-gradient flat-plate boundary layer. *J. Fluid Mech.* **630**, 5–41.
- WYGNANSKI, I. J., SOKOLOV, M. & FRIEDMAN, D. 1976 On a turbulent 'spot' in a laminar boundary layer. *J. Fluid Mech.* **78**, 785–819.
- WYGNANSKI, J., ZILBERMAN, M. & HARITONIDIS, J. H. 1982 On the spreading of a turbulent spot in the absence of a pressure gradient. *J. Fluid Mech.* **123**, 69–90.